Understanding Marker-Based Normalization for FLIM Networks

Leonardo de Melo Joao[1,2][a], Matheus Abrantes Cerqueira[1][b], Barbara Caroline Benato[1][c] and Alexandre Xavier Falcao[1][d]

[1]*Institute of Computing, State University of Campinas, Campinas, 13083-872, São Paulo, Brazil*

[2]*LIGM, Univ. Gustave-Eiffel, Marne-la-Valée, F-77454, France*

Keywords: Marker-Based-Normalization, Flim, Z-Score-Normalization, Object-Detection.

Abstract: Successful methods for object detection in multiple image domains are based on convolutional networks. However, such approaches require large annotated image sets for network training. One can build object detectors by exploring a recent methodology, Feature Learning from Image Markers (FLIM), that considerably reduces human effort in data annotation. In FLIM, the encoder's filters are estimated among image patches extracted from scribbles drawn by the user on discriminative regions of a few representative images. The filters are meant to create feature maps in which the object is activated or deactivated. This task depends on a z-score normalization using the scribbles' statistics, named marker-based normalization (MBN). An adaptive decoder (point-wise convolution with activation) finds its parameters for each image and outputs a saliency map for object detection. This encoder-decoder network is trained without backpropagation. This work investigates the effect of MBN on the network's results. We detach the scribble sets for filter estimation and MBN, introduce a bot that draws scribbles with distinct ratios of object-and-background samples, and evaluate the impact of five different ratios on three datasets through six quantitative metrics and feature projection analysis. The experiments suggest that scribble detachment and MBN with object oversampling are beneficial.

1 INTRODUCTION

Object detection has been widely studied in computer vision with several applications (Kaur and Singh, 2022). Object detection is commonly used for estimating (and often classifying) bounding boxes around objects. Alternatively, Salient Object Detection (SOD) methods are suitable for single-class tasks — minimum bounding boxes can be estimated around the salient objects (Joao et al., 2023). We adopt this second approach. The best-performing methods are based on deep neural networks, mostly Convolutional Neural Networks (CNNs) (Zaidi et al., 2022). However, they require considerable computational resources and human effort in data annotation.

Human effort and computational resources can be significantly reduced with a recent methodology named Feature Learning by Image Markers (FLIM) for training convolutional encoders without backpropagation (De Souza and Falcão, 2020). In FLIM, the user draws scribbles on discriminative regions of very few (e.g., 5) representative images. The encoder's filters of the first convolutional layer are estimated from patches centered at scribble pixels. The process repeats for each subsequent layer by mapping the scribbles onto the output of the previous one. For a single-class object detection problem, each filter is meant to activate the object or background (Figure 1). The success of this task depends on a z-score normalization using the scribbles' statistics, named marker-based normalization (MBN). Such foreground and background activations favor using a single-layer decoder (point-wise convolution with activation) that adapts the weights for each image and outputs a saliency map suitable for object detection. In (Joao et al., 2023), the authors explore this methodology to create flyweight encoder-decoder networks for object detection with competitive results to fully pretrained deep models.

A patch centered at a pixel can be represented by a vector with the attributes of its pixels. The dot product between a filter's weight vector and each image patch corresponds to the convolution operation. The lower the angle between filter and patch vectors, the higher the dot product between them (i.e., the similarity be-

[a] https://orcid.org/0000-0003-4625-7840
[b] https://orcid.org/0000-0003-3655-3435
[c] https://orcid.org/0000-0003-0806-3607
[d] https://orcid.org/0000-0002-2914-5380

Joao, L., Cerqueira, M., Benato, B. and Falcao, A.
Understanding Marker-Based Normalization for FLIM Networks.
DOI: 10.5220/0012385900003660
Paper published under CC license (CC BY-NC-ND 4.0)
In *Proceedings of the 19th International Joint Conference on Computer Vision, Imaging and Computer Graphics Theory and Applications (VISIGRAPP 2024) - Volume 2: VISAPP*, pages 612-623
ISBN: 978-989-758-679-8; ISSN: 2184-4321
Proceedings Copyright © 2024 by SCITEPRESS – Science and Technology Publications, Lda.

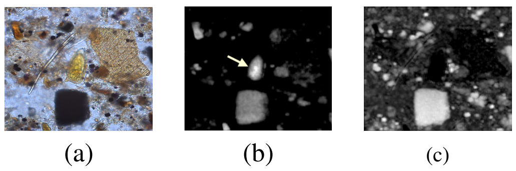

Figure 1: Foreground and background filter activations on a parasite egg image. (a) Original Image; (b-c) Foreground and Background activations. An yellow arrow points the object of interest.

tween their visual patterns). The patches extracted from the scribbles may form distinct groups in a patch feature space. MBN aims to centralize the groups and correct distortions among attributes. In FLIM, each group center generates one filter. For foreground and background activations, MBN should increase the angle between such groups as much as possible.

Figure 2.a illustrates four groups of patches such that filters from groups green and red generate simultaneous and redundant activation maps. MBN aims to create group distributions, as depicted in Figure 2.b, which presents higher angular distances among the groups. Estimating the z-score normalization parameters from the scribbles' statistics is crucial to achieving that aim due to the natural imbalance between the numbers of foreground and background patches within an image. Z-score normalization using statistics from all pixels would likely create a group distribution, as depicted in Figure 2.c, where the less dense classes' statistics are not considered.

Understanding the impact of drawing more or fewer markers in the foreground or background for MBN can guide users' actions when building the network. However, FLIM uses the same scribble set for filter estimation and MBN. In this work, we investigate the impact of MBN on the network results for object detection by detaching the parts of the scribbles used for each operation. No studies so far have addressed the role of MBN in the network construction process.

For this study, we developed a marker bot to draw disks in the foreground and background parts and extend them into scribbles inside each part. Scribble drawing is a controlled process such that we can generate a distinct ratio between object and background patches. We evaluate the impact of MBN using three datasets, five different ratios – balanced (1:1) and imbalanced (1:10, 1:50) for both background and foreground –, and six metrics of object detection with visual analysis of feature space projections (Zeiler et al., 2014; Rauber et al., 2017). Additionally, we compare the results with the traditional FLIM in which filter estimation and MBN use the same scribble set.

The contributions of this paper are four-fold: (i) understanding the isolated impact of MBN within FLIM networks using metrics and visualization; (ii) understanding the impact of different foreground-and-background ratios when learning the normalization parameters for FLIM networks; (iii) a mathematical interpretation of the role of (marker-based) normalization in creating feature spaces suitable for convolution; and (iv) a marker bot for drawing scribbles based on ground truth masks for training FLIM networks.

2 RELATED WORK

The literature has a range of approaches to normalization that vary in complexity and robustness to outliers, such as min-max, which is simpler but significantly impacted by outliers, and z-score, which uses the mean and deviation as measures of location and scale. Tanh-estimators are less sensitive to outliers but require parameter configuration(Jain et al., 2005). There is no consensus on a single method (Omar et al., 2022), but z-score normalization is very relevant as it is one of the most common normalization methods.

Z-score normalization assumes the data to be normally distributed (Jain et al., 2005), which often is not the case in images with a large imbalance of foreground and background pixels (as discussed in Figure 2). To circumvent that problem, MBN was proposed and user-drawn scribbles were used to undersample the data for learning the normalization parameters (De Souza and Falcão, 2020).

MBN was used in several works together with FLIM CNNs, and is suitable for classification (De Souza and Falcão, 2020), object detection (Joao et al., 2023), and segmentation tasks (Sousa et al., 2021; Cerqueira et al., 2023) in multiple image domains. However, none of these methods studied the impact of different scribble sets for the normalization parameters. In this work, we propose to analyze that impact by looking at feature space projections and the object detection result of an encoder-decoder network.

3 BACKGROUND

In this section, we provide the definitions required for our proposal and discussions (Section 3.1), an overview of how to train FLIM networks for object detection (Section 3.2), a formalization of the Marker-based normalization (Section 3.3), and some mathematical interpretations of convolutions, dot product and the normalization impact for creating feature

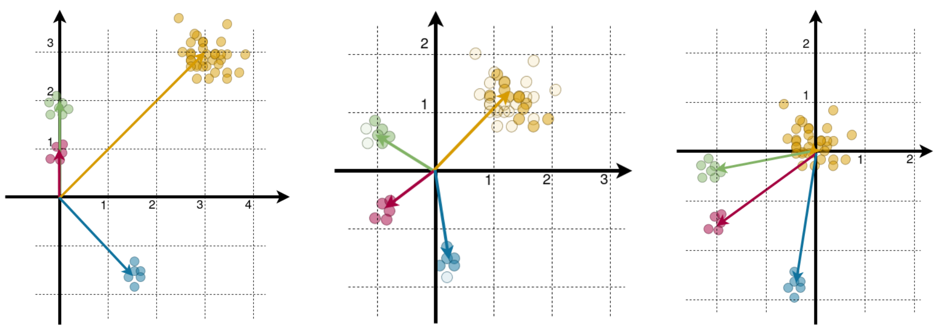

(a) (b) (c)

Figure 2: Impacts of normalization: (a) original space; (b) desired normalization; (c) z-score normalization of entire data.

spaces suitable for these operations (Section 3.4).

3.1 Definitions

Images, Adjacency Relations, and Image Patches: Let an image be defined by $\mathbf{X} \in \mathbb{R}^{h \times w \times c}$ where $h \times w$ are its dimension with c number of channels. Considering $i \in \{1,h\}, j \in \{1,w\}$, a pixel at position (i,j) can be seen as its feature vector $\mathbf{x}_{ij} \in \mathbb{R}^c$, with its b-th channel (feature) value being $x_{ijb} \in \mathbb{R}, b \in \{1,c\}$.

Let $u \in \{1,h\}, v \in \{1,w\}$, and $p = (i,j), q = (u,v)$ be the coordinates of image pixels. An adjacency relation $\mathcal{A}$ can be defined as a binary translation-invariant relation between pixels (p,q). In this work, two adjacency relations are used. For annotating the scribbles, we use a circular relation $\mathcal{A}_c$ with radius $\rho \geq 0$, which is defined by $\mathcal{A}_c : \{(p,q) | \ \|q-p\| \leq \rho\}$.

For the convolution operations and kernel estimations, we use image patches contained within a square relation $\mathcal{A}_s$ of size $a \geq 0$, defined by $\mathcal{A}_s : \{(p,q) | \ |x_q - x_p| \leq a, |y_q - y_p| \leq a\}$.

In any case, $\mathcal{A}(p)$ is a set of pixels $q \in \mathbb{Z}^2$ adjacent to p. Zero-padding is done so all image pixels to have the same size for their adjacency relations.

Lastly, an image patch $\mathbf{p}_p \in \mathbb{R}^{a \times a \times c}$, is a sub-image with the c features of all $a \times a$ pixels in $\mathcal{A}_s(p)$.

Filters and Convolutions. A kernel (or filter) $\mathbf{k} \in \mathbb{R}^{a \times a \times c}$ is a matrix with the same shape as a patch. Within a CNN, the convolution of an image with a filter can be described as $\mathbf{Y} = \mathbf{X} \star \mathbf{k}$. Assuming zero padding, $\mathbf{Y} \in \mathbb{R}^{h \times w \times 1}$ and $y_{ij} \in \mathbf{Y}$.

Let $\mathbf{p}_p$ and $\tilde{\mathbf{k}}$ be represented as flattened vectors $\tilde{\mathbf{p}}_p, \tilde{\mathbf{k}} \in \mathbb{R}^d$, such that $d = a \cdot a \cdot c$. The value of y_p can be computed by the dot product between the kernel and patch vectors:

$$\begin{aligned} y_{ij} &= \langle \tilde{\mathbf{p}}_p, \tilde{\mathbf{k}} \rangle \qquad (1) \\ \text{with } \langle \tilde{\mathbf{p}}_p, \tilde{\mathbf{k}} \rangle &= \|\tilde{\mathbf{p}}_p\| \|\tilde{\mathbf{k}}\| \cos\theta, \end{aligned}$$

where θ is the angle between both vectors.

3.2 FLIM Networks

FLIM is a methodology to create feature extractors (encoders) to compose convolutional blocks of CNNs. In FLIM, kernels are estimated from image patches centered on marked pixels, which are also used to learn the normalization parameters. The FLIM encoders can be combined with different decoders to provide successful image classification, segmentation, and object detection solutions. In this section, we first present the steps for training a FLIM encoder (Section 3.2.1) and how we can combine it with an Adaptive Decoder to propose a solution for object detection tasks (Section 3.2.2).

3.2.1 Encoder Learning

FLIM has been described to contain six steps (Joao et al., 2023):

1. **Training Image Selection** - For this work, we follow the same strategy as (Joao et al., 2023) and manually selected a small number of representative images (1% of the dataset) such that the training set contains examples of the most visually distinguishing characteristics among the object class.
2. **Marker Drawing** - Markers have to be drawn in the training images. We use the proposed marker-bot (Section 4.1).
3. **Data Preparation** - Marker-based normalization is applied, and the markers are scaled onto the required image dimension for the layer. This is the step we are investigating further in this work.
4. **Kernel Estimation** - Given the training images, a pre-defined architecture, and image markers, the convolutional kernels are extracted, respecting the sizes and numbers defined in the architecture. For learning the kernels, given an image marker, we cluster all its marker patches (patches centered on its pixels) using k-means and take the centers of

each of the k_m clusters found as a kernel. Then, the total number of kernels is reduced using another K-means to fit the required number of filters in the defined architecture for a given layer.

5. **Block Execution** - Every image goes through the transformations within the learned convolutional block, and the new image features are extracted. These operations are usually convolution, activation — commonly the Rectified Linear Unit (ReLU) (Nair and Hinton, 2010) —, and pooling.
6. **Kernel Selection** - One may select kernels to reduce redundancy, simplifying the network. We do not explore kernel selection in this work.

After each convolutional block is learned, steps 3-6 are repeated until the desired network architecture is achieved, with the previous output being used as the input for learning the kernels of the next block.

3.2.2 FLIM CNN and Adaptive Decoder

Recently, an unsupervised and adaptive decoder (Joao et al., 2023) was proposed for creating flyweight (tiny) CNNs, allowing the creation of fully connected networks for object detection without the need of backpropagation.

The adaptive decoders proposed so far are simply one-layer point-wise convolutions followed by a ReLU, where the kernel weights are estimated on the fly according to the input image and an adaptation function. Point-wise convolution can be understood as a weighted sum of all image channels of the input image. Let $\mathbf{A} \in \mathbb{R}^{h' \times w' \times m}$ be the output of an encoder's layer, where h', w' are the image image's height and width after pooling, and $\alpha = [\alpha_1, \alpha_2, ..., \alpha_m] \in \mathbb{R}^m$ be the convolutional weights, such that $\alpha_b \in [-1, 1]$, and $b = 1, 2, \ldots, m$. The decoder is than simply $\mathbf{S} = ReLU(\langle \mathbf{A}, \alpha \rangle)$.

As mentioned, the decoder weights are estimated by an adaptation function, which is a heuristic based on prior information about the image domain. For the target problems, the background is often larger and somewhat homogeneous, so the adaptation function defines a kernel to be positive if it has a low mean activation value. Let $F : \alpha_b \to \{-\alpha, 0, \alpha\}$ be the adaptation function, such that:

The literature has a range of approaches to normalization that vary in complexity and robustness to outliers, such as min-max, which is simpler but significantly impacted by outliers, and z-score, which uses the mean and deviation as measures of location and scale. Tanh-estimators are less sensitive to outliers but require parameter configuration(Jain et al., 2005). There is no consensus on a single method (Omar et al., 2022), but z-score normalization is very relevant as it is one of the most common normalization methods.

$$\mathbf{F}(\mathbf{A}, b) = \begin{cases} +\alpha, & \text{if } \mu_{\mathbf{A}_b} \leq \tau_{\mathbf{A}_b} + \sigma_\mu \\ -\alpha, & \text{if } \mu_{\mathbf{A}_b} \geq \tau_{\mathbf{A}_b} - \sigma_\mu \\ 0, & \text{otherwise.} \end{cases}$$

where $\tau_{\mathbf{A}_b}$ is the Otsu threshold computed for all the means, $\bar{\mu} = \frac{1}{m}\sum_{b=1}^{m} \mu_{\mathbf{A}_b}$ and $\sigma_\mu = \frac{1}{m}\sum_{b=1}^{m}(\mu_{\mathbf{A}_b} - \bar{\mu})^2$. By assuming the background and foreground mean activations to be split between two densities, the Otsu is used here to find the separation between them.

The decoder outputs a saliency map that, for the purpose of object detection, can be thresholded using the Otsu method so that minimum bounding boxes can be set around the binary connected components. Combining a FLIM encoder with an unsupervised adaptation encoder provides a weak supervised approach for object detection, where the only annotations required are the scribbles from a few training images.

3.3 Marker-Based Normalization

When learning the Z-score normalization parameters, FLIM uses the estimated markers to undersample the data. That operation is called Marker-based Normalization (MBN).. Let $\mathcal{X}$ be the set of training images (the ones containing markers), where an image is denoted by $\mathbf{X} \in \mathcal{X}$, and its marker set by $\mathcal{M}(\mathbf{X})$. Also, let $\mathcal{M}$ be the set of all markers, such that $\bigcup_{\mathbf{X} \in \mathcal{X}} \mathcal{M}(\mathbf{X})$. An image $\mathbf{X}$ can be normalized into $\hat{\mathbf{X}} \in \mathbb{R}^{h \times w \times m}$, by the following equation:

$$\hat{x}_{ijb} = \frac{x_{ijb} - \mu_b}{\sigma_b + \varepsilon}, \tag{2}$$

where $\mu_b = \frac{1}{|\mathcal{M}|} \sum_{\forall x_{ijb} \in \mathcal{M}(\mathbf{X})} x_{ijb}$, is the mean of the marker features, $\sigma_b^2 = \frac{1}{|\mathcal{M}|} \sum_{\forall x_{ijb} \in \mathcal{M}(\mathbf{X})} \left(x_{ijb} - \mu_b\right)^2$ is their standard deviation, and $\varepsilon > 0$ is a small constant.

3.4 Mathematical Interpretations

Starting from the convolution operation, as discussed in (Joao et al., 2023), the dot-product (in Equation 1) can be interpreted geometrically as a projection of $\tilde{\mathbf{p}}_{ij}$ into a hyperplane $\mathbf{h}$ positioned at the origin of $\mathbb{R}^d$ that is perpendicular to $\tilde{\mathbf{k}}$ (Figure 3). This projection can be seen as a similarity measure scaled by the vectors' magnitudes. However, it is essentially a signed angular (cosine) distance, where the sign depends on which side of the hyperplane $\tilde{\mathbf{p}}_{ij}$ is.

By considering convolution as a similarity function, in FLIM, kernels are estimated as the center of the marked-patch clusters. The intuition is that these vectors are representatives of the texture related to said cluster so that a convolution operation with said kernel creates a high similarity value in image regions with textures similar to the ones this kernel represents. A kernel extracted from a marker placed in a discriminating object texture is expected to have high similarity to that same texture in other images.

However, because the dot-product similarity is scaled by the vector magnitudes, a high convolutional value does not imply that the vectors are close in the feature space. In Figure 3.a, the vector $\overrightarrow{k}$ is the one that defines the hyperplane H, but the highest dot product similarity is not with itself but with a vector with higher magnitude and smaller angular similarity ($\overrightarrow{q}$). Note that, after normalization (Figure3.b), the angles between vector pairs are often increased, and the vector's magnitudes are controlled, providing a space much more suitable for using the dot product as a similarity function. That is precisely why we understand normalization as an essential operation for convolutional neural networks.

Nevertheless, in highly unbalanced data, regular z-score normalization might not achieve the desired result. Take the example in Figure 2.b, where one cluster is more densely populated. The data's mean and standard deviation will likely spread the dense cluster around the center and disregard the others. By doing so, the angular distance among the important clusters does not necessarily change.

MBN proposes a solution to such a problem. By undersampling the data to only the patches within marker pixels, the mean and standard deviation learned are more likely to achieve a better spread of the clusters that represent the textures that are important according to the user annotation (Figure 2.c).

4 PROPOSED ANALYSIS

In this paper, we propose understanding the impact of different ratios of data undersampling for learning the normalization parameters in FLIM-based CNNs. To do so, we implemented a marker bot to be able to control the proportion of samples between the background and foreground (Section 4.1) and modify FLIM to allow the learning of the normalization parameters and of the kernels to be done with two different marker sets (Section 4.2) and propose an analysis methodology for understanding the impact of the different sample ratios in the encoded feature space and the decoded bounding box predictions (Section 4.3).

4.1 Marker Bot with Controlled Ratio

To create marker sets specifically for MBN, the proposed marker bot requires three inputs: (i) an image $\mathbf{I} \in \mathbb{R}^{h\times w\times 3}$; (ii) the number of desired markers per class (n), and (iii) the ratio between object and background pixels. Within this paper, this ratio is denoted by $fg : bg$, where $fg \in \mathbb{N}^+$ refers to the ratio of foreground samples (pixels) and $bg \in \mathbb{N}^+$ of background ones. At the end, the bot outputs a marker set for each training image, respecting the desired number of markers and sample ratio.

Given the input, the marker bot performs three operations: (1) Sample representative regions; (2) Draw disk marker; (3) Extend the markers to scribbles.

Sample Representative Regions. Assuming objects can be heterogeneous, we want to draw markers in all distinctive object characteristics. For such, we each image label is executed at a time, so, let $Q_l \in \mathbb{R}^{n_l\times 3}$ be a set with all pixel feature vectors of a given label, where $l = \{0,1\}$ denoting either background (0) or foreground (1), n_l be the number of pixels for each label, $q \in Q_l$, and $Coord : q \to (ij)$, considering $(ij) \in \mathbf{I}$.

The distinct regions in label are found by k-means (MacQueen et al., 1967) clustering each set Q_l, where k clusters are found and a cluster is attributed to each pixel $q \in Q_l$, so $c_{ij} \in [0,k]$ denotes which cluster (ij) belongs to, and $c_{ij} = 0$ if $Coord(q) = (ij)$ and $q \notin Q_l$. For each cluster, we draw a marker in the center of its largest connected component. When $k = n$, no further operations are needed, and when $k > n$ we only add markers in the n largest clusters. However, when $k < n$, we draw $\frac{n}{k}$ markers in each cluster, and $\frac{n}{k} + n\%k$ on the largest one.

When estimating more than one marker per cluster, we create a center-focus priority map $W\mathbb{R}^{n_l\times 1}$, such that $w_q \in [0,1] = d(q,q_c)$, where $q_c = (q_c,q_c)$ is the center of the component and $d(q,q_c) = \frac{(|i-i_c)|+|(j-j_c)|}{area}$, with $area$ being the area of the component q_c belongs to. Then, a marker is added on the pixel with highest priority q, and all its neighbors have their priority decreased (Figure 4), so that $w_p = w_p * d(p,q), \forall p \in \mathcal{A}_s(q)$ — in this work we used an adjacency size of $a = 0.1 * area$.

Draw Disk Marker. Given a pixel selected from a discriminating region and a marker size ρ, we validate if that pixel can be a marker center and if so, we draw a maker in its adjacency, adding it to the marker set. Let $M \in R^2$ be the marker set, p be a pixel, and an adjacency $\mathcal{A}_c(p)$, where $label(q) = \{0,1\}$ determine the label of a pixel, and $label(p) = l$. A marker is added to the set if all of its pixels are within the image domain, possesses the same label as the center pixel, and

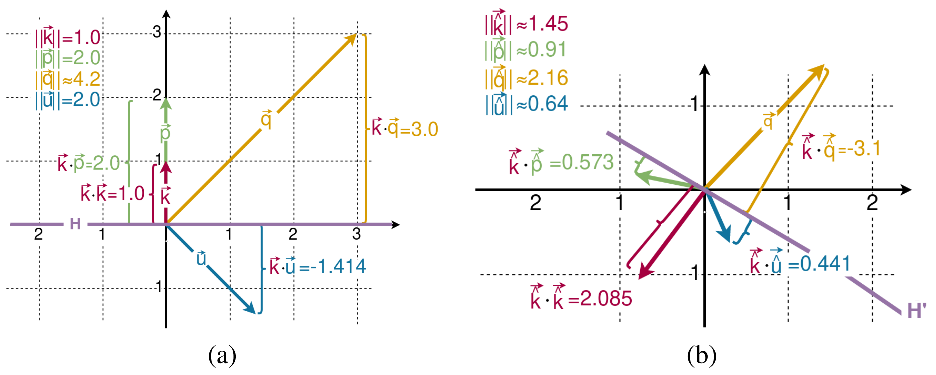
$||\vec{k}||=1.0$
$||\vec{p}||=2.0$
$||\vec{q}||\approx4.2$
$||\vec{u}||=2.0$
$\vec{k}\cdot\vec{p}=2.0$
$\vec{k}\cdot\vec{k}=1.0$
$\vec{k}\cdot\vec{q}=3.0$
$\vec{k}\cdot\vec{u}=-1.414$
H
(a)
$||\vec{k}||\approx1.45$
$||\vec{p}||\approx0.91$
$||\vec{q}||\approx2.16$
$||\vec{u}||\approx0.64$
$\vec{k}\cdot\vec{p}=0.573$
$\vec{k}\cdot\vec{q}=-3.1$
$\vec{k}\cdot\vec{u}=0.441$
$\vec{k}\cdot\vec{k}=2.085$
H'
(b)

Figure 3: Dot product as a similarity between vectors: (a) illustrates the hyperplane H defined by an given vector $\vec{k}$ and its dot product to other vectors; (b) shows the same vectors after normalization.

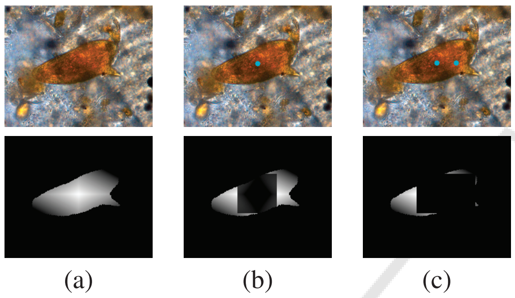

Figure 4: Center-focused weight and penalization at each iteration. Original images with estimate markers on the top, and weight maps on the bottom. The images are cropped to improve visualization. (a-c) Iterations 0, 1 and 2.

none of them are already part of another marker, *i.e.*, $\forall q \in \mathcal{A}_c(p), label(q) = l, q \in \mathbf{I}, q \notin M \rightarrow M \bigcup \mathcal{A}_c(p)$. If the conditions are not met, the marker is not added and another pixel must be found to be used as as marker center. That verification function is named $valid\_marker()$ in Algorithm 1. Also, to facilitate the extension of the markers to scribbles, a marker set $M* \subset M$ is created simultaneously, containing only the center of each marker.

Extend Markers to Scribbles. Marker extension to scribbles starts from a set of marker center $M*$, an image domain $\mathbf{I}$, a ratio of increase, and an adjacency size ρ. Then, for each marker center in the marker set, we select a random valid direction to start the marker growing — A direction is deemed valid if the marker centered on the next pixel is valid according to $valid\_marker()$. The marker grows in that direction until it achieves half of the desired proportion, then. The same process happens in the opposite direction in order to respect the center of the marker (Figure 5).

In cases where the marker cannot grow until the desired proportion, the marker selects a new direction to keep growing. If there is no possible direction, the bot stops without achieving the exact number. If the early stoppage happens in the first direction, the second one will try to compensate for the loss in size. The algorithm goes as follows:

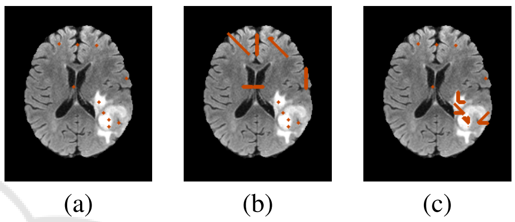

Figure 5: Marker extension to scribbles. (a) Markers, (b-c) scribbles for background and foreground, respectively.

4.2 FLIM with Multiple Marker Sets

To learn the FLIM networks, we modify FLIM to allow different scribble sets to learn the kernels and the normalization parameters. As shown in Figure 6, the training images are annotated by the marker bot, which provides two different sets, with Scribble Set 1 being used to estimate the kernels, and Scribble Set 2 being used to learn the normalization parameters in MBN. Multiple iterations of the Data Prep., Kernel Estimation and Layer Execution are performed to learn the FLIM encoder, which is combined with the adaptive decoder to provide the object detection solutions that are evaluated.

After the decoder, a bi-cubic interpolation scales the output back to the original image's domain, an Otsu threshold binarizes the saliency, and minimum bounding-boxes are estimated around each connected component. In all datasets, we discard bounding boxes with sizes smaller than 0.5% of the image's area to handle small noise components.

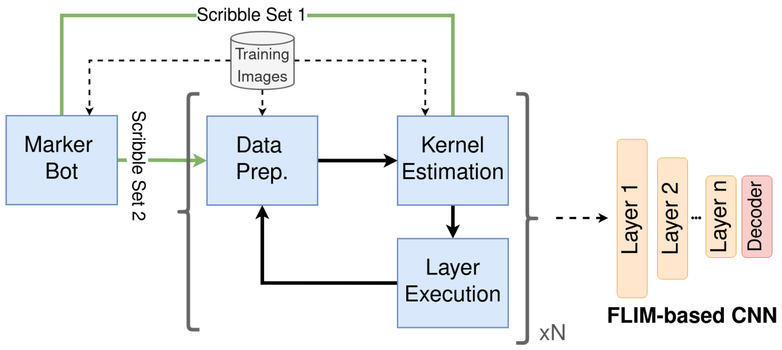

Figure 6: Pipeline for learning FLIM networks with multiple scribble sets.

Algorithm 1: Extend to scribbles.

```
Data: $M*, \mathbf{I}, ratio, \rho$
Result: $M+$
$M+ \leftarrow \{\}$;
$size \leftarrow len(M*)$;
foreach $p \in M$ do
    $goal \leftarrow (len(M) * ratio)/2$;
    $q \leftarrow p$;
    $dir\_list = get\_available\_dir(q)$;
    $dir \leftarrow random\_dir(dir\_list)$;
    $initial\_dir \leftarrow dir$;
    for $i \leftarrow 0$ to $1$ do
        while $size < goal || len(dir\_list) > 0$ do
            $v \leftarrow q + dir$;
            $m \leftarrow adjacency(v, \rho)$;
            if $valid\_marker(m)$ then
                $add\_marker(M+, m)$;
                $q \leftarrow v$;
                $size \leftarrow size + len(m)$;
            end
            else
                $dir\_list = get\_available\_dir()$;
                $dir \leftarrow random\_dir(dir\_list)$;
            end
        end
        $dir \leftarrow intial\_dir * -1$;
        $goal \leftarrow goal * 2$
    end
end
```

4.3 Evaluation

In order to evaluate the multiple scribble sets, we propose (i) different proportions of samples in the background and foreground and (ii) analysing the impact of the MBN along layers in the architecture of a FLIM network. Additionally, we can analyze both (i) and (ii) considering the decoder's and encoder's output in a FLIM network. Next, we describe the proposed evaluations when considering both outputs.

4.3.1 Decoder

Although we have an intuition of the desired feature space for convolutions, we do not know how the normalized convolutional feature space impacts object detection decoders. So, we propose evaluating a FLIM CNN with adaptive decoders (as presented in Section 6) using traditional metrics for positive bounding box predictions. Because the decoder estimates the weights on the fly, it can be used in the output of each convolutional layer, allowing an analysis layer-by-layer (ii). Doing so with different sample ratios allows us to analyze each ratio's impact on the decoded results (i).

4.3.2 Encoder

To evaluate the impact of (i) and (ii) in the encoder without bias in the decoder's quality, we propose using t-SNE (van der Maaten and Hinton, 2008) to reduce the many dimensions output from a convolutional layer to create 2-d projections. T-SNE was selected because it has shown positive results when explored to generate valuable insights about network behavior for human analysis(Rauber et al., 2017).

In short, consider $\mathbf{A} \in \mathbb{R}^{h\times w\times m}$ to be a layer's output after pooling and interpolating back to the original image domain. T-SNE maps a sample (pixels) in the multi-dimensional feature space to a 2-D feature vector, , for $p \in \mathbf{A}'$, $tSNE : p \in \mathbb{R}^m \rightarrow p_2 \in \mathbb{R}^2$. Then, a color is attributed to every pixel in the new feature space to identify whether the pixel belongs to the foreground or background.

Because the projections are independent of the decoder's quality, we intend to analyze them to see how normalization impacts the resulting feature space and if the observations correlate to the decoder results.

5 EXPERIMENTS

5.1 Experimental Setup

Foreground/Background Imbalancing Setups. We ran experiments with a balanced number of samples (1:1), a considerably imbalanced ratio (1:10, 10:1), and a large imbalance (1:50, 50:1). For larger imbalances, some images did not achieve the exact number due to lack of space inside the objects. We use "*d*" to determine models that detach the normalization marker set for each step. Therefore, if the results state **50:1 Layer1d**, we are looking at the first layer of a model learned with different marker sets, were for normalization, a proportion of 50:1 foreground-to-background was used. In the detached case, the imbalance occurred only during normalization, with the filters being estimated with the disk markers.

Datasets. We used three dataset:

1. *Schistosoma Mansoni* eggs dataset (**Schisto**): A proprietary microscopy dataset (Santos et al., 2019) composed of 631 images of *S. mansoni* eggs with an often cluttered background, where the objects of interest can be partially occluded;
2. A subset of the ship detection dataset (Dadario, 2018) (**Ships**) composed of 463 aerial images of ships (images out of the 621 from the original dataset). We removed images containing ships smaller than 1% of the image to remove the challenging drastic scale difference;
3. (**Brain**) A subset of a proprietary glioblastoma dataset (Cerqueira et al., 2023) composed of 1326 slices (images out of the 44 three-dimensional images of the original dataset). The slices were extracted from the axial axis, using a stride equal to 2 and removing a percentage of removing a percentage of both ends (12%). The subset was composed of slices of FLAIR (Fluid attenuated inversion recovery) sequence of Magnetic Resonance Imaging that shows the tumor as an active area.

Network Architecture. We fixed the same network architecture for all datasets, and the architecture is depicted in Figure 7. To understand the feature spaces created rather than finding the best model for each dataset, we tested the decoder at the end of every layer for every experiment. It is worth noting that all pooling had a stride factor of two.

Parameters. For FLIM, the number of kernels per marker is fixed to 5 in all layers. For the marker bot, 5 markers were estimated for each label in each image. The adjacency radius for marker size varied from $\rho = \{4, 4, 2\}$ for the **Schisto**, **Ships**, and **Brain** datasets, respectively — the variation is due to a large size difference in the image and the objects' areas.

Evaluation Metrics. We have two analyses of our results: (i) The object detection results given by the decoded features after the adaptive decoder; (2) a feature space projection analysis of the encoded features. The former provides insight into the ratio's impact in networks with an adaptive decoder, and the latter evaluates the feature space with no decoder bias.

We propose using four distinct object detection metrics based on positive and negative bounding box predictions to evaluate the decoded features. A bounding box is a positive prediction if it has an Intersection over Union (IoU) (Rezatofighi et al., 2019) score greater than a threshold τ to an uncounted ground-truth object. Based on the number of positive and negative predictions, we compute the precision and recall and derive the following metrics: the F_2-score, the Precision-Recall (PR) curve, the Average Precision, and the mean Average Precision. The F_2-score is a weighted harmonic mean of the precision and recall, favoring recall over precision. The PR curve varies the IoU threshold to measure the achievable precision for each possible recall level. The Average Precision (AP^{τ}) is the Area Under the Curve of the PR-curve up to a given threshold τ, and the Mean Average Precision (μAP) is a good overall metric for object detection being the mean AP over thresholds varying from $\tau \in [0.5, 0.55, ..., 0.95]$.

5.2 Results from Decoded Features

Considering the results for the decoded layers, Table 1 shows the best results for each ratio setup in each dataset. For the Schisto and Brain datasets, foreground oversampling produced the best overall results; balanced sampling produced intermediate ones and background oversampling was substantially worse (also seen in the PR curves in Figure 9). Oversampling creates a better representation of individual structures within that class, and because both datasets have considerably heterogeneous backgrounds, the decoder highlights background objects that activate isolated, increasing the number of false positives (Figure 8.a-b). For the ships dataset, the best result was achieved by oversampling the background, although the difference was considerably less significant than it was on the other two datasets. Similar to the previous analysis but with an opposite effect, the oversampled class has more regions activating individually, which is detrimental for the foreground in this dataset with higher variability of textures and colors within the same object. Figure 8.c shows an example of an event that happened with some frequency where the object was detected but split into parts.

Regarding the impact of the markers in the nor-

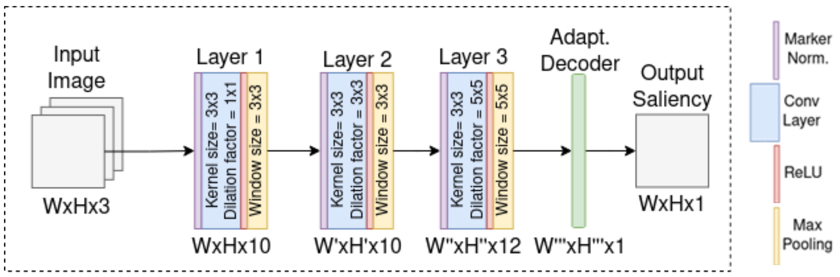

Figure 7: Architecture of trained networks.

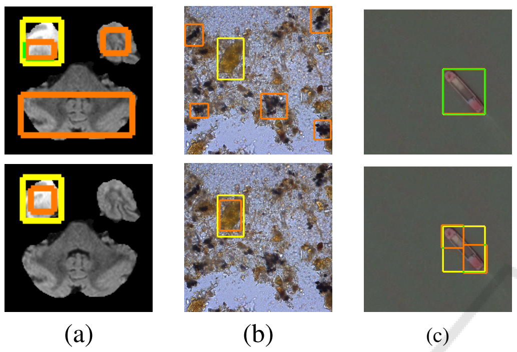

Figure 8: Difference in detection predictions on different ratios. On the top, results with a ratio of (10:1), and on the bottom (1:10). (a-c) Brain, Schisto and Ships, respectively.

Table 1: Best results for each proportion. The two best results for each metric are in blue and green, respectively.

Schisto	$F_2^{0.5}$	$AP^{0.5}$	$F_2^{0.75}$	$AP^{0.75}$	μAP
50:1 (Layer 1d)	0.744	0.663	0.530	0.280	0.364
10:1 (Layer 1d)	0.756	0.682	0.568	0.352	0.385
1:1 (Layer 1)	0.634	0.431	0.467	0.221	0.250
1:10 (Layer 2)	0.464	0.393	0.276	0.234	0.217
1:50 (Layer 2)	0.512	0.356	0.270	0.173	0.185
Ships	$F_2^{0.5}$	$AP^{0.5}$	$F_2^{0.75}$	$AP^{0.75}$	μAP
50:1 (Layer 1d)	0.722	0.722	0.529	0.529	0.460
10:1 (Layer 1d)	0.740	0.743	0.517	0.518	0.464
1:1 (Layer 1)	0.764	0.770	0.564	0.568	0.503
1:10 (Layer 1d)	0.774	0.768	0.584	0.579	0.507
1:50 (Layer 1d)	0.779	0.778	0.588	0.586	0.510
Brain	$F_2^{0.5}$	$AP^{0.5}$	$F_2^{0.75}$	$AP^{0.75}$	μAP
50:1 (Layer 2)	0.642	0.624	0.248	0.106	0.260
10:1 (Layer 2)	0.591	0.576	0.236	0.230	0.252
1:1 (Layer 2)	0.585	0.564	0.189	0.159	0.249
1:10 (Layer 2d)	0.094	0.059	0.017	0.002	0.019
1:50 (Layer 2)	0.398	0.355	0.105	0.058	0.135

malization alone, Table 2 shows the mean and standard deviation of all ratios for each decoded layer. A large standard deviation means the results change significantly depending on the ratio. That is evidence that normalization has a meaningful impact on the model's performance. Also, having multiple results from detached marker sets achieving a higher performance than regular FLIM (Layer 1d for Schisto and Brain and all layers from ships) indicates that using separate marker sets might be beneficial. A combination of user-drawn scribbles for kernel learning and their automatic extension for providing a controlled sampling ratio could be explored for future work.

Also, note that Layer 3 had an inferior performance in all datasets. That is primarily due to a considerable reduction in the image size after both stridden pooling and creating maps where the difference of mean activation was negligible, so the decoder could not perform correctly. A more complex decoder might be required to exploit multiple layers better.

Table 2: Mean and standard deviation over all sampling proportions for each layers. The two best results for each dataset are highlighted in blue and green, respectively.

Schisto	$F_2^{0.5}$	$AP^{0.5}$	$F_2^{0.75}$	$AP^{0.75}$	μAP
Layer 1	0.475±0.220	0.381±0.188	0.316±0.158	0.172±0.065	0.196±0.089
Layer 1d	0.511±0.251	0.417±0.233	0.367±0.193	0.210±0.100	0.234±0.130
Layer 2	0.548±0.069	0.419±0.064	0.319±0.039	0.183±0.028	0.214±0.024
Layer 2d	0.539±0.109	0.400±0.096	0.324±0.084	0.173±0.027	0.203±0.049
Layer 3	0.314±0.196	0.191±0.147	0.068±0.054	0.019±0.016	0.066±0.052
Layer 3d	0.304±0.162	0.181±0.129	0.062±0.051	0.024±0.020	0.064±0.050
Ships	$F_2^{0.5}$	$AP^{0.5}$	$F_2^{0.75}$	$AP^{0.75}$	μAP
Layer 1	0.745±0.015	0.702±0.086	0.506±0.060	0.404±0.176	0.403±0.096
Layer 1d	0.756±0.022	0.756±0.021	0.556±0.029	0.556±0.027	0.489±0.022
Layer 2	0.553±0.114	0.501±0.140	0.282±0.144	0.201±0.194	0.231±0.123
Layer 2d	0.575±0.094	0.504±0.148	0.321±0.115	0.244±0.172	0.251±0.128
Layer 3	0.282±0.145	0.229±0.172	0.071±0.047	0.013±0.010	0.071±0.058
Layer 3d	0.328±0.145	0.242±0.200	0.094±0.049	0.021±0.012	0.079±0.069
Brain	$F_2^{0.5}$	$AP^{0.5}$	$F_2^{0.75}$	$AP^{0.75}$	μAP
Layer 1	0.178±0.129	0.147±0.132	0.055±0.041	0.033±0.029	0.063±0.054
Layer 1d	0.269±0.146	0.211±0.130	0.099±0.072	0.038±0.032	0.085±0.053
Layer 2	0.459±0.207	0.428±0.223	0.159±0.087	0.111±0.079	0.181±0.098
Layer 2d	0.345±0.163	0.315±0.167	0.115±0.061	0.090±0.061	0.132±0.077
Layer 3	0.030±0.031	0.011±0.014	0.003±0.004	0.000±0.000	0.002±0.003
Layer 3d	0.034±0.032	0.011±0.014	0.003±0.004	0.000±0.000	0.002±0.003

As presented in Table 3, the variance among different layers considering the same foreground-to-background proportion is not very high for the ratios that provided an adequate result (blue and green), apart from the $F^{0.5}$ and $AP^{0.5}$ in the brain dataset. That is likely because this dataset is more challenging, and appropriate solutions are achieved only at the second layer, resulting in a significant difference in results. In most images of that dataset, layer one can detect only a partial part of the tumor, while Layer 2 has a much more homogeneous activation.

The ships dataset had the most negligible impact among different setups (also in Table 3) where oversampling the background was better than doing it for the foreground. That is likely due to the homogeneity of the background within most images in the dataset, making it easier to isolate non-background regions by better characterizing the background instead of isolating regions with high similarity to the foreground.

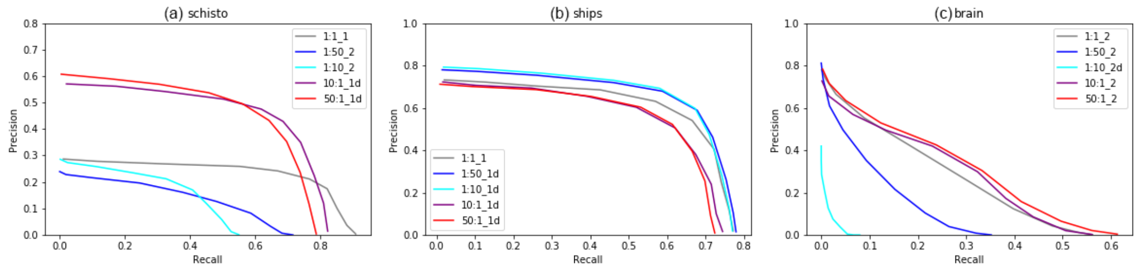

Figure 9: Precision-Recall curves for each dataset considering the best performing layer for each sampling ratio. In the caption 1:10_1d means the results come from 1:10 proportion, layer 1 and detached marker sets. (a) Schisto; (b) Ships; (c) Brain.

Table 3: Mean and standard deviation of Layers 1, 1d, 2, 2d for each sampling proportion. The two best results for each metric in each dataset are in blue and green, respectively.

Schisto	$F_2^{0.5}$	$AP^{0.5}$	$F_2^{0.75}$	$AP^{0.75}$	μAP
50:1	0.681±0.036	0.575±0.052	0.427±0.063	0.216±0.046	0.290±0.043
10:1	0.667±0.058	0.545±0.095	0.449±0.076	0.234±0.071	0.280±0.064
1:1	0.574±0.060	0.401±0.030	0.398±0.069	0.200±0.021	0.222±0.028
1:10	0.289±0.133	0.225±0.119	0.172±0.072	0.129±0.066	0.120±0.064
1:50	0.381±0.120	0.275±0.069	0.210±0.056	0.144±0.023	0.146±0.032
Ships	$F_2^{0.5}$	$AP^{0.5}$	$F_2^{0.75}$	$AP^{0.75}$	μAP
50:1	0.583±0.142	0.570±0.153	0.335±0.176	0.226±0.191	0.273±0.137
10:1	0.607±0.136	0.517±0.145	0.320±0.151	0.201±0.188	0.243±0.136
1:1	0.649±0.114	0.560±0.210	0.412±0.152	0.327±0.241	0.323±0.181
1:10	0.724±0.042	0.716±0.046	0.520±0.058	0.513±0.061	0.450±0.047
1:50	0.723±0.039	0.716±0.042	0.495±0.058	0.490±0.061	0.429±0.054
Brain	$F_2^{0.5}$	$AP^{0.5}$	$F_2^{0.75}$	$AP^{0.75}$	μAP
50:1	0.394±0.182	0.350±0.188	0.163±0.064	0.091±0.045	0.148±0.077
10:1	0.333±0.213	0.296±0.206	0.128±0.088	0.096±0.084	0.124±0.090
1:1	0.458±0.127	0.438±0.126	0.152±0.036	0.116±0.043	0.191±0.058
1:10	0.078±0.014	0.025±0.021	0.014±0.004	0.001±0.001	0.008±0.007
1:50	0.302±0.095	0.267±0.087	0.077±0.035	0.036±0.022	0.105±0.032

5.3 Feature Projection Analysis

Analyzing all possible combinations of feature spaces from the proposed experiments of Sec. 5.2 would be unfeasible. For each dataset, we proposed to evaluate five foreground and background proportions (50:1, 10:1, 1:1, 1:10, and 1:50) and feature spaces of the output of three distinct layers. Additionally, each dataset contains hundreds of samples, and each image contains thousands of pixels. Projecting pixels of all images in a dataset would result in a projection with millions of points. Due to that, we select one image from the experiment with a large variation in $F_2^{0.5}$ among layers and sample ratio. We then project the encoder's output related to this image in the 2D space. Results for both comparisons are given below.

5.3.1 Different Foreground-to-Background Ratio

Image-space projections of one image per dataset are shown in Figure 10. Blue points are foreground pixels, and red points are background. For each dataset (rows), different proportions for background and foreground markers are presented (columns).

For *Schisto*, one can notice a big and dense cloud of background points with some foreground ones mixed into the cloud (in the middle right of the large cloud). For 50:1, 10:1, and 1:1, a small group of red points is separated from the blue cloud while another is attached. For 1:10 and 1:50, there is no clear separation between the blue cloud of points and any group of red points. This visual hint is confirmed by the quantitative results obtained by the decoder in Table 3, which shows better results for proportions of 50:1 and 10:1.

For *Schips*, a big and dense cloud of blue points (background) is entirely separated from a small group of red points (foreground). There is no mixture between red and blue points in the projections. Again, this visual hint agrees with the quantitative results obtained by the decoder in Table 3, but the non-substantial increase in background oversampling is most likely due to decoder limitations rather than a less suitable feature space.

For *Brain*, a semi-circle of blue points and some groups of blue points are observed in all projections of distinct proportions. Also, there is a group of red points in the tail of the semi-circle of the blue points. For 50:1 and 10:1, the group of red points is more compact. Particularly, for 1:10, the spread of red points over the semi-circle of blue points is larger. That also agrees with the results in Table 3.

Additionally, analysing distinct datasets, the projections with a clear separation between classes are the ones that provided better results for the object detection metric, where *Ships* had the highest results, followed by *Schisto* and lastly *Brain*.

5.3.2 Along Layers

Figure 11 shows image space projections of one image per dataset. For distinct datasets (rows), the output of distinct layers is presented (columns).

For *Schisto* and *Ships*, a dense cloud of blue points is separated from a small group of red points in *layer 1*, although there is more mixture of red points in the bottom right of the blue cloud for the *Schisto* dataset. On *layer 2*, *Schisto* still presents a similar separation to the first layer, but there is more mixture for *Ships*. These observations align with the average behavior described in Table 2, where the results from the first

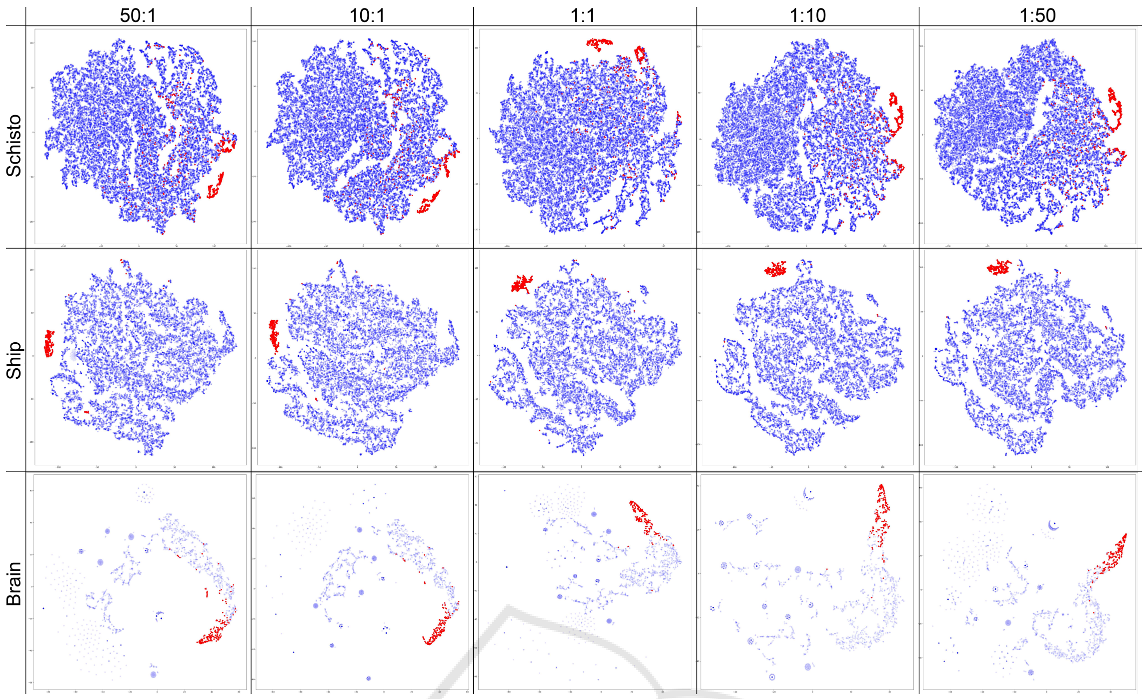

Figure 10: 2D projected image spaces for a single image in each dataset. Each point in the projection refers to a pixel whose color indicates whether it is from the background (blue) or foreground (red). Opacity of blue samples is set to show the number of samples overlapping.

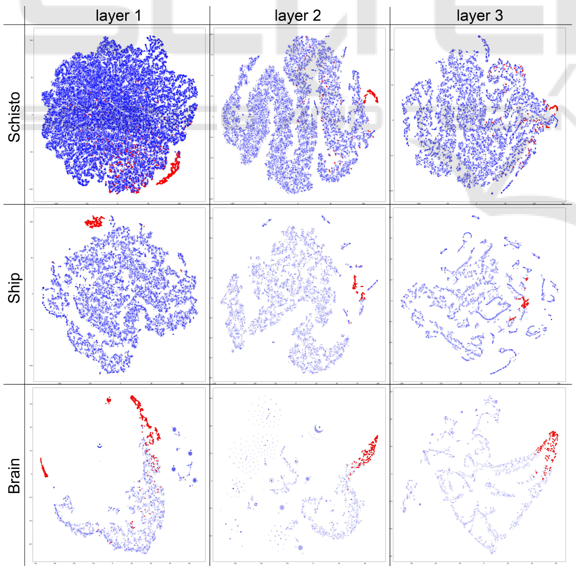

Figure 11: 2D projected image spaces for a single image in each dataset and for different layers. Each point refers to a pixel whose color indicates whether it is from the background (blue) or foreground (red). Opacity of blue samples is set to show the number of samples overlapping.

two layers are similar for the *Schisto* dataset but a larger degradation for the second layer on *Ships*. In *layer 3*, the separation is no longer seen in either case.

For *Brain*, in *layer 1*, most blue points are grouped in a semi-circle with a tail of red points with no clear separation between them, and small groups of isolated red and blue points are seen. In *layer 2*, red points are in a single and more clustered group, with less mixture among red and blue points compared to the other layers, which was the layer with better results in Table 2. No semi-circle structure of blue points is present in *layer 3*, as seen in the other layers. Red points are also more spread out and not in a dense and small group.

Also, when comparing projections for distinct datasets, one can notice that the best projection for any layer – in which red groups (foreground) are more separated from blue points (background) – is given by *Ship, layer 1*, *Schisto, layer 2*, and *Brain, layer 2* in this order, which is in line with the best quantitative results for the decoder evaluation in Table 1. The visual separation between foreground and background points in the 2D projection also follows the same trend as the adaptative decoder. As a result, this experiment shows a *positive* correlation between the separation of points of foreground and background of distinct layers in a 2D projection and qualitative results of an adaptative decoder.

6 CONCLUSION

We evaluated the impact of different marker sets when learning the normalization parameters of FLIM networks for object detection. For this analysis, we modified the FLIM methodology to allow one marker set to be used when estimating the kernels and another when computing the normalization parameters. We also introduced a marker bot to create FLIM CNNs automatically from ground truth with a desired proportion of foreground-to-background ratio.

Our analysis showed a positive correlation between 2D projections and our adaptive decoder, opening ways to build encoders more suitable for FLIM networks without needing a decoder for layer evaluation. The results showed that different normalization parameters have significant impact and oversampled classes provide a better representation of their object parts, allowing the design of a more accurate, high-quality, and interpretable FLIM network.

For future work, user-drawn markers could be used to create better-positioned markers for learning the kernels, and then they could be extended automatically to learn the normalization parameters in the desirable unbalanced setup to provide better solutions. Also, a similar study could be developed with the detached marker sets to understand better the impact of different markers for kernel estimation, having a fixed set for normalization.

ACKNOWLEDGEMENTS

The authors thank the financial support from Coordenação de Aperfeiçoamento de Pessoal de Nível Superior – Brasil (CAPES) with Finance Code 001, CAPES COFECUB (88887.800167/2022-00), CNPq (303808/2018-7), FAEPEX, and Labex Bézout/ANR.

REFERENCES

Cerqueira, M. A., Sprenger, F., Teixeira, B. C., and Falcão, A. X. (2023). Building brain tumor segmentation networks with user-assisted filter estimation and selection. In *18th International Symposium on Medical Information Processing and Analysis*, volume 12567, pages 202–211. SPIE.

Dadario, A. M. V. (2018). Ship detection from aerial images. https://www.kaggle.com/datasets/andrewmvd/ship-detection.

De Souza, I. E. and Falcão, A. X. (2020). Learning cnn filters from user-drawn image markers for coconut-tree image classification. *IEEE Geoscience and Remote Sensing Letters*.

Jain, A., Nandakumar, K., and Ross, A. (2005). Score normalization in multimodal biometric systems. *Pattern recognition*, 38(12):2270–2285.

Joao, L. d. M., Santos, B. M. d., Guimaraes, S. J. F., Gomes, J. F., Kijak, E., Falcao, A. X., et al. (2023). A flyweight cnn with adaptive decoder for schistosoma mansoni egg detection. *arXiv preprint arXiv:2306.14840*.

Kaur, J. and Singh, W. (2022). Tools, techniques, datasets and application areas for object detection in an image: a review. *Multimedia Tools and Applications*, 81(27):38297–38351.

MacQueen, J. et al. (1967). Some methods for classification and analysis of multivariate observations. In *Proceedings of the fifth Berkeley symposium on mathematical statistics and probability*, volume 1, pages 281–297. Oakland, CA, USA.

Nair, V. and Hinton, G. E. (2010). Rectified linear units improve restricted boltzmann machines. In *Proceedings of the 27th international conference on machine learning (ICML-10)*, pages 807–814.

Omar, N., Supriyanto, E., Wahab, A. A., Al-Ashwal, R. H. A., and Nazirun, N. N. N. (2022). Application of k-means algorithm on normalized and standardized data for type 2 diabetes subclusters. In *2022 International Conference on Healthcare Engineering (ICHE)*, pages 1–6. IEEE.

Rauber, P. E., Fadel, S. G., Falcão, A. X., and Telea, A. (2017). Visualizing the hidden activity of artificial neural networks. *IEEE TVCG*, 23(1).

Rezatofighi, H., Tsoi, N., Gwak, J., Sadeghian, A., Reid, I., and Savarese, S. (2019). Generalized intersection over union: A metric and a loss for bounding box regression. In *Proceedings of the IEEE/CVF conference on computer vision and pattern recognition*, pages 658–666.

Santos, B. M., Soares, F. A., Rosa, S. L., Gomes, D. d. C. F., Oliveira, B. C. M., Peixinho, A. Z., Suzuki, C. T. N., Bresciani, K. D. S., Falcao, A. X., and Gomes, J. F. (2019). Tf-test quantified: a new technique for diagnosis of schistosoma mansoni eggs. *Tropical Medicine & International Health*.

Sousa, A. M., Reis, F., Zerbini, R., Comba, J. L., and Falcão, A. X. (2021). Cnn filter learning from drawn markers for the detection of suggestive signs of covid-19 in ct images. In *2021 43rd Annual International Conference of the IEEE Engineering in Medicine & Biology Society (EMBC)*.

van der Maaten, L. and Hinton, G. (2008). Visualizing data using t-SNE. *JMLR*, 9:2579–2605.

Zaidi, S. S. A., Ansari, M. S., Aslam, A., Kanwal, N., Asghar, M., and Lee, B. (2022). A survey of modern deep learning based object detection models. *Digital Signal Processing*, page 103514.

Zeiler, M. D., Fergus, R., Fleet, D., Pajdla, T., Schiele, B., and Tuytelaars, T. (2014). *Visualizing and Understanding Convolutional Networks*, pages 818–833. Springer International Publishing, Cham.